Ab initio simulations of the dynamic ion structure factor of warm dense lithium

B. B. L. Witte, M. Shihab, S. H. Glenzer, and R. Redmer

Phys. Rev. B **95**, 144105 — Published 6 April 2017

DOI: 10.1103/PhysRevB.95.144105

Ab initio simulations of the dynamic ion structure factor of warm dense lithium

B.B.L. Witte,[1,2] M. Shihab,[1,3] S.H. Glenzer,[2] and R. Redmer[1]

[1] *Universität Rostock, Institut für Physik, D-18051 Rostock, Germany*
[2] *SLAC National Accelerator Laboratory, 2575 Sand Hill Road, MS 72 Menlo Park, CA 94025 USA*
[3] *Department of Physics, Faculty of Science, Tanta University, Tanta 31527, Egypt*

(Dated: March 6, 2017)

We present molecular dynamics simulations based on finite-temperature density functional theory that determine self-consistently the dynamic ion structure factor and the electronic form factor in lithium. Our comprehensive data set allows for the calculation of the dispersion relation for collective excitations, the calculation of the sound velocity, and the determination of the *ion feature* from the total electronic form factor and the ion structure factor. The results are compared with available experimental x-ray and neutron scattering data. Good agreement is found for both the liquid metal and warm dense matter domain. Finally, we study the impact of possible target inhomogeneities on x-ray scattering spectra.

PACS numbers: 52.65.Yy, 52.35.Dm, 52.25.-b, 61.20.-p, 47.11.Mn

I. INTRODUCTION

The physics of warm dense matter (WDM) i.e. matter at solid-state-like density and beyond with temperatures of a few to tens of eV is of lively interest. This state challenges many-particle theory since strong ion-ion correlations and partially degenerate electrons prohibit simplified treatments, e.g., by using perturbation theory. Furthermore, WDM is relevant for astrophysics, e.g., for interior, evolution, and dynamo models of giant planets [1–3], and for inertial confinement fusion research [4, 5]. The dynamic structure factor (DSF), the spectral function of the density-density correlations in the system, is of fundamental importance for theoretical models of WDM and is needed to determine equation of states (EOS) and the transport properties. Furthermore, the differential scattering cross section of x-rays focused onto a charged particle system (liquid metal, WDM, or hot dense plasma) is determined by the DSF of the electrons [6]. Thereby, the DSF is accessible via laboratory experiments using brilliant x-ray sources, generated by powerful optical lasers [7] or using free electron lasers (FELs) [8] in x-ray Thomson scattering (XRTS) experiments.

The differential cross section for XRTS in the Born approximation is given by the total dynamic structure factor of the electrons $d^2\sigma/(d\omega d\Omega) = \sigma_T S_{\rm ee}^{tot}(\vec{k},\omega)$. Here $\hbar\vec{k}$ and $\hbar\omega$ are respectively the transferred momentum and energy in the scattering process of x-rays by electrons. $S_{\rm ee}^{tot}$ denotes the total dynamic structure factor. The Chihara formula for the total DSF is widely used for the evaluation of XRTS spectra [6, 9]; it reads as [10]:

$$S_{\rm ee}^{tot}(\vec{k},\omega) = Z_{\rm f} S_{\rm ee}^{0}(\vec{k},\omega) + |N(\vec{k})|^2 S_{\rm ii}(\vec{k},\omega), \qquad (1)$$

when contributions from bound-free and bound-bound transitions are neglected. The first term –the *electron feature*, $S_{\rm ee}(\vec{k},\omega) = Z_{\rm f} S_{\rm ee}^{0}(\vec{k},\omega)$– describes the DSF of free electrons with $Z_{\rm f}$ being the number of quasi-free electrons per nucleus. In collective XRTS configurations, the electron feature provides plasmon modes from which one can derive plasma parameters such as the electron density and electron temperature, employing the detailed balance and the plasmon dispersion relation [6, 11, 12]. Recently, also the electrical conductivity was extracted from the collisionally-damped plasmon feature [13]. In the non-collective regime, the electron feature shows the Compton down-shifted response which reflects the electron velocity distribution along the scattering vector. The second term –the *ion feature*, $S_{\rm ee}^{\rm i}(\vec{k},\omega) = |N(\vec{k})|^2 S_{\rm ii}(\vec{k},\omega)$– gives the contribution of electrons following the ion motion. Its amplitude, $|N(\vec{k})|^2$, is the total form factor of the electronic structure around the nuclei. The correlations in the ion system are usually described via the dynamic ion structure factor $S_{\rm ii}(k,\omega)$ applying classical integral equation techniques [14] or molecular dynamics (MD) simulations [15].

For simple liquids, the dynamic ion structure factor is often approximated using the hydrodynamic model [16–19], where $S_{\rm ii}(k,\omega)$ forms the well-known Rayleigh-Brillouin triplet. Hence, the *ion feature* is then composed of the central Rayleigh peak due to the scattering on the electron structure $N(k)$ following the diffusive ion motion (i.e., thermal diffusion mode) and the Stokes and Anti-Stokes side peaks of the Brillouin scattering, i.e., ion acoustic modes. The two ion acoustic modes are shifted typically with few tens of meV. The DSF has been measured in the liquid metal regime, i.e., for aluminum [20] or lithium [21, 22] but also for liquid neon [23, 24] or liquid argon [25]. These measurements are of fundamental importance for the determination of the structure and, especially, the dynamics of the ion system, which enable the calculation of the sound speed via the dispersion relation or the ion temperature. Fortunately, new x-ray sources such as the Linear Coherent Light Source

(LCLS) and the European XFEL, with their high peak brightness and excellent signal-to-noise ratio, will allow measurements of this triplet and of the electron feature in the WDM regime [26] at the same time, which determines the ion temperature and electron temperature, respectively. As a consequence, the non-equilibrium dynamics between electrons and ions on ultra-short time scales will be revealed experimentally using XRTS.

In this work, we present *ab initio* results for the DSF of the ions in liquid and warm dense lithium using finite-temperature density functional theory molecular dynamics (DFT-MD) simulations. The corresponding dispersion relations of ion acoustic modes are derived. Our results for the DSF and the dispersion relation in the liquid metal and WDM regimes agree with experimental results. Furthermore, we calculate the *ion feature* in warm dense lithium for the conditions of an XRTS experiment [27] using exclusively the data from the DFT-MD runs. In this way, we can drop assumptions that were made for the evaluation of the experimental data and extract the plasma parameters consistently. In particular we find an ionization state of 1.0 in warm dense lithium which is lower than inferred in [27]. Finally, we check the effect of inhomogeneities [28] in the optically pumped, warm dense lithium target on the electron feature and calculate the ionization state based on the results of radiation-hydrodynamic simulations using a more realistic equation of state, where pressure ionization is considered. In addition, we propose to check the predicted dynamic properties of warm dense lithium in future high-resolution experiments at FELs.

II. THEORETICAL METHOD

We first concentrate on the structure and dynamics of the ionic system which are described by $S_{\mathrm{ii}}(k,\omega)$, see the second term in Eq. (1). With the knowledge of the ion density in Fourier space $\rho^{\mathrm{i}}_{\vec{k}}(t) = \sum_{v=1}^{N} \mathrm{e}^{-i\vec{k}\cdot\vec{r}_v(t)}$ and the number of ions N we can define the intermediate scattering function $F^{\mathrm{c}}_{\mathrm{ii}}(\vec{k},t)$ as

$$F^{\mathrm{c}}_{\mathrm{ii}}(\vec{k},t) := \frac{1}{N}\lim_{T\to\infty}\frac{1}{T}\int_0^T \rho^{\mathrm{i}}_{\vec{k}}(\tau)\rho^{\mathrm{i}}_{-\vec{k}}(\tau+t)d\tau\,, \quad (2)$$

$$S^{\mathrm{c}}_{\mathrm{ii}}(\vec{k},\omega) := \frac{1}{2\pi}\int_{-\infty}^{\infty} F^{\mathrm{c}}_{\mathrm{ii}}(\vec{k},t)\mathrm{e}^{i\omega t}\mathrm{d}t\,. \quad (3)$$

In the limit of free particles, the DSF reads as

$$S^{\mathrm{c}}_{\mathrm{ii}}(k,\omega) = \sqrt{\frac{m_{\mathrm{i}}\beta}{2\pi k^2}}e^{-\frac{m_{\mathrm{i}}\beta\omega^2}{2k^2}}\,, \quad (4)$$

assuming a Maxwell-Boltzmann velocity distribution function with $1/\beta = k_B T_i$, where m_{i}, k_{B}, T_i denote the ion mass, Boltzmann constant, and the ion temperature, respectively.

In order to describe the scattering signal the electronic system has to be characterized. The quantum treatment of electrons in DFT-MD simulations enables the calculation of the electron density $\rho^{\mathrm{e}}(\vec{r})$ via the single-electron Kohn-Sham wave functions ϕ_n,

$$\rho^{\mathrm{e}}(\vec{r}) = \sum_n f_n \left|\phi_n(\vec{r})\right|^2, \quad (5)$$

with f_n being the Fermi occupation number of states n with energy ϵ_n; the corresponding Fourier transform is ρ^{e}_k. On the other hand, ions in our DFT-MD simulation are treated classically. The total form factor $N(\vec{k})$ is calculated by averaging over the time steps of the simulation [29],

$$N(\vec{k}) = \lim_{\tau\to\infty}\frac{1}{\tau}\int_0^\tau \frac{\rho^{\mathrm{e}}_{\vec{k}}(t)}{\rho^{\mathrm{i}}_{\vec{k}}(t)}\mathrm{d}t\,. \quad (6)$$

In the long-wavelength limit $N(k\to 0) = Z$ follows by definition. Switching to the chemical picture, N(k) can be split to contributions from different electronic states. As we find from our calculations a large energy band gap of ~ 41 eV between the K- and L-shell in lithium it is meaningful to express the total form factor as a sum of contributions of bound and quasi-free states: $N(\vec{k}) = f(\vec{k}) + q(\vec{k})$. We use $\rho^{\mathrm{e}}(\vec{r}) = \rho^{\mathrm{e}}_{\mathrm{b}}(\vec{r}) + \rho^{\mathrm{e}}_{\mathrm{f}}(\vec{r})$, which yields $f(\vec{k})$ (the bound form factor) and $q(\vec{k})$ (the screening cloud) using Eq. (6), respectively [29].

The DFT-MD calculations were performed with the Vienna *ab initio* simulation package VASP [30–32] using the provided projector augmented wave [33, 34] pseudopotential for the interaction between the nuclei and the electrons. We used the exchange-correlation functional of Perdew, Burke, and Ernzerhof [35]. The electron wave functions are expanded into plane waves up to a cutoff energy of 500 to 1000 eV. For the interaction between ions and electrons a projector augmented-wave potential [33] is used, in which all three electrons per lithium atom are described in the DFT framework. All MD simulations were carried out using 64 ions and ran for a minimum of 15000 time steps after equilibration. As a time step for the ion motion in the MD we used 1.5 fs and 0.8 fs for the liquid and the warm dense domain, respectively. The convergence of the results has been checked with regard to the number of particles, energy cutoff, Brillouin zone sampling, and the number of time steps. To control the temperature the algorithm of Nosé [36] is used with a Nosé mass corresponding to a temperature oscillation period of about 40 time steps. The sampling of the Brillouin zone was carried out at the Baldereschi mean value point [37]. In the following, only isotropic systems are considered. Therefore, we report only quantities averaged over the possible wave vectors with the same magnitude.

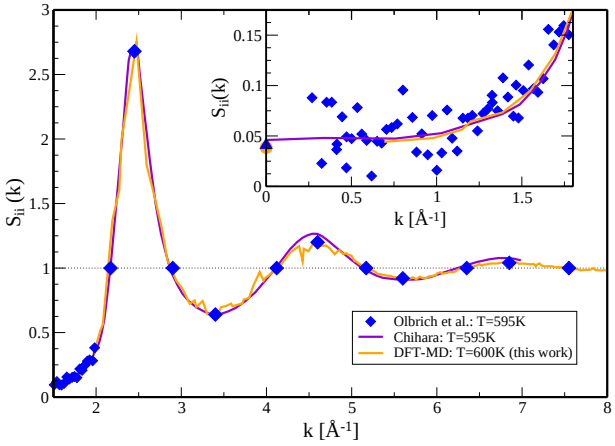

Figure 1. Static structure factor $S_{ii}(k)$ for liquid lithium at $T = 0.495$ g/cm^3 from scattering experiments of Olbrich *et al.* [38] at $T = 595$ K (blue diamond), from an analytical model of Chihara [39] (violet line), and from DFT-MD simulations at $T = 600$ K (orange line). In the inset, the long-wavelength limit is shown via the isothermal compressibility as determined from separate DFT-MD simulations for $T = 600$ K (orange circle) and experimental values [38] (blue triangle).

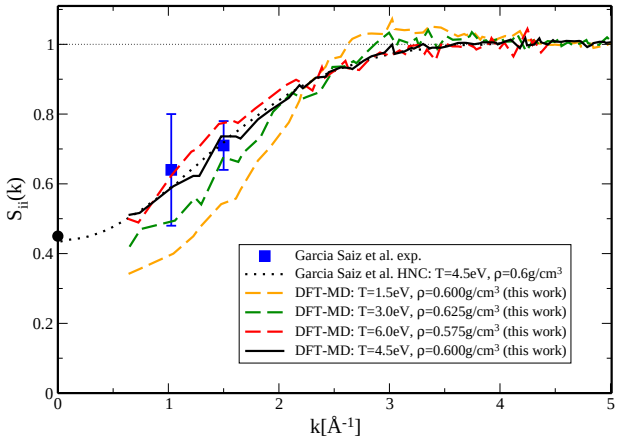

Figure 2. Static structure factor $S_{ii}(k)$ from x-ray scattering experiments [27] for warm dense lithium at $T = 4.5 \pm 1.5$ eV and $\rho = 0.6 \pm 0.025$ g/cm^3 (blue boxes) and corresponding DFT-MD simulation results of this work (black solid line) with the long-wavelength limit from DFT-MD simulations (black circle). We also show the results for the density and temperature varied within the experimental error bars (red and green dashed lines) and one result for stronger correlated lithium (orange dashed line). An ionization degree of $Z_f = 1.35$ is estimated and used in the HNC calculations of Ref. [27] (black dotted line), while $Z_f = 1.0$ is determined from DFT-MD in this work.

III. RESULTS FOR THE STATIC ION STRUCTURE FACTOR

The static structure factor is obtained via the intermediate scattering function $S_{ii}(k) = F^c_{ii}(k, 0)$ from Eq. (2). In Fig. 1, we compare our simulation results at 600 K (∼0.05 eV) with available data from neutron and x-ray scattering experiments [38] performed at $T = 595$ K and a mass density of 0.495 g/cm^3 which represents an ion number density of $n = 0.043$ Å^{-3}. The melting point is at 453 K. Our simulation results agree very well with the experimental data of Olbrich *et al.* [38] for all k values and with an analytical model of Chihara [39]. Furthermore, in the long-wavelength limit, $S_{ii}(k \to 0)$ can be calculated via the isothermal compressibility κ_T by

$$S_{ii}(k \to 0) = n_i k_B T \kappa_T, \qquad \kappa_T = -\frac{1}{V}\left(\frac{\partial V}{\partial p}\right)_T . \tag{7}$$

The isothermal compressibility in this work is determined from the EOS calculated via separate DFT-MD runs. Olbrich *et al.* [38] report a long-wavelength limit $S_{ii}(k \to 0) = 0.041$ using neutron and also x-ray scattering which agrees well with our result $S_{ii}(k \to 0) = 0.039$. The error bars in our compressibility values $S_{ii}(k \to 0)$ are smaller than the point size.

García Saiz *et al.* [27] recently performed a pump-probe experiment on shock-compressed lithium, where an estimated ion density of (0.0521 ± 0.002) Å^{-3} [mass density of (0.6 ± 0.025) g/cm^3] and a temperature of (4.5 ± 1.5) eV [(52220 ± 17407) K] via XRTS were extracted. They reported also on the static structure factor. In Fig. 2, we find a good agreement of the *ab initio* calculated $S_{ii}(k)$ for $T = 4.5$ eV and $\rho = 0.6$ g/cm^3 with the experimental data. In addition, we studied the changes of the static ion structure factor with respect to the given error-bars for the density and temperature [27] and still find agreement. The corresponding coupling parameters Γ defined as the ratio of the Coulomb energy to the thermal energy are given in Tab. I. They vary from strongly correlated systems ($\Gamma \gg 1$) to weakly correlated systems ($\Gamma \sim 1$). For clarity reasons, the ion structure factor for a system with $\Gamma = 6$ is shown for which in $S_{ii}(k)$ a slight peak follows. In addition, the calculated long-wavelength limit $S_{ii}(k \to 0) = 0.45$ for $T = 4.5$ eV and $\rho = 0.6$ g/cm^3 is consistent with the hypernetted chain calculation (HNC) with a screened Coulomb potential reported in [27].

IV. RESULTS FOR THE DYNAMIC ION STRUCTURE FACTOR

We get access to $S^c_{ii}(k, \omega)$ via the intermediate scattering function $F^c_{ii}(k, t)$ from Eq. (2). In the case of liquid lithium, Scopigno *et al.* [22, 40, 41] determined and discussed the dynamic ion structure factor via x-ray scattering experiments at $T = 600$ K. Due to the finite simu-

lation box, it is challenging to perform DFT-MD simulations at equal k values as given in the experiment. Therefore, we calculated the DSF on a fine grid of wave vectors, then interpolated the DSF at the k values given in the experiment. The grid spacing is fine enough to allow linear interpolation. The classical quantity $S_{\rm ii}^{\rm c}(k,\omega)$ obtained from DFT-MD simulations is multiplied with a prefactor to take care of detailed balance effects in scattering processes (not associated with particle correlations). Hence, the DSF $S_{\rm ii}(k,\omega)$ is

$$S_{\rm ii}(k,\omega) = \frac{1-\exp(-\beta\hbar\omega)}{\beta\hbar\omega} S_{\rm ii}^{\rm c}(k,\omega)\ . \qquad (8)$$

In this work, negative frequency shifts have the meaning of a down-shifted frequency for an incoming and scattered photon. Fig. 3 shows $S_{\rm ii}(k,\omega)$ for different k values for liquid lithium, a central Rayleigh peak and two ion acoustic modes are observed. For all wave vectors our simulation shows reasonable agreement with the experiment [22]. However, for all scattering angles the calculated central mode seems to be lower and broader compared to the experiment. This feature has been observed before [42]. In future work the DSF can be used to determine more material properties from the hydrodynamic model [19, 43, 44] or an extended hydrodynamic model [45] and in this sense check a possible influences of the used thermostat [46], which has to be further benchmarked; i.e. against available measurements of dense liquids [20–25].

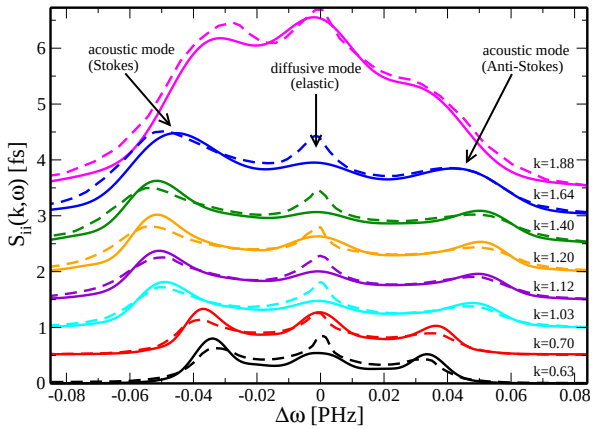

Figure 3. DSF $S_{\rm ii}(k,\omega)$ of liquid lithium versus frequency shift at $T = 600$ K and $\rho = 0.513$ g/cm^3. Dashed lines: experimental data from x-ray scattering [22]; solid lines: DFT-MD results of this work. Each set of curves is shifted by a constant offset of 0.5 fs with respect to the lower one. The position of the ion acoustic mode determines the dispersion relation.

We report also on the DSF of warm dense lithium for different wave vectors in Fig. 4. For $k = 0.64$ Å^{-1} we obtain the known triplet. For larger k values, the ion

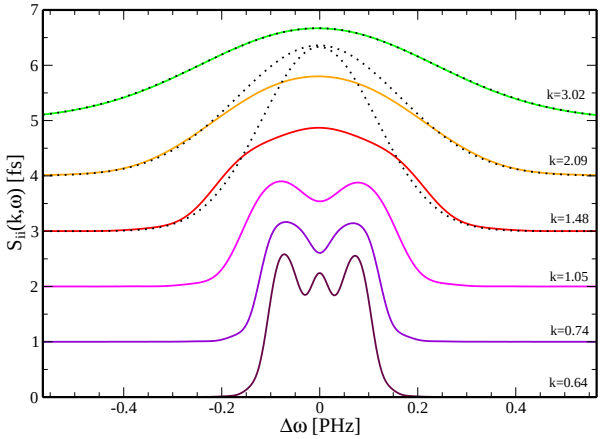

Figure 4. DSF $S_{\rm ii}(k,\omega)$ of warm dense lithium versus frequency shift at $T = 4.5$ eV and $\rho = 0.6$ g/cm^3 from DFT-MD simulations. Each set of curves is shifted by a constant offset of 1.0 fs with respect to the lower one. The wave vectors at 1.05 Å^{-1} and 1.48 Å^{-1} correspond to the scattering angles of 40° and 60° in the x-ray scattering experiment [27]. Dotted lines represent the free particle limit.

Table I. Adiabatic (c_s) and apparent sound velocity (c_l) for liquid and warm dense lithium deduced from a linear fit to the dispersion relation at small wave vectors.

Te	ϱ [g/cm^3]	Γ	$c_{\rm s}$ [m/s]	$c_{\rm l}$ [m/s]
600 K (∼0.05 eV)	0.495	157	5126	5085
17407 K (∼1.50 eV)	0.600	6	9017	9111
34813 K (∼3.00 eV)	0.625	3	11875	11891
52220 K (∼4.50 eV)	0.600	2	13538	13640
69627 K (∼6.00 eV)	0.575	1	15691	15329

acoustic modes are shifted to higher frequencies due to dispersion. The calculated dynamic ion structure factor for $k = 3.02$ Å^{-1} (and also higher k values) is consistent with the free particle limit; non-collective scattering is dominant.

The experimentally determined and the calculated DSFs show an asymmetry due to quantum effects, i.e., detailed balance; Eq.(8). For the smallest considered wave vector in Figs. 3 and 4, the intensity of the Stokes mode is 50% and 1% higher than the anti-Stokes mode, respectively. Hence, the ion temperature could in principle be extracted from the asymmetry between the ion acoustic modes in the DSF. Obviously, this becomes challenging with increasing temperature. However, extremely bright and narrow x-ray sources like the European XFEL [47] or the LCLS [48, 49] operated in the seeded beam mode could be used to determine the ion acoustic modes in WDM with high resolution and, thereby, measure the ion temperature independently from the electron temperature via XRTS.

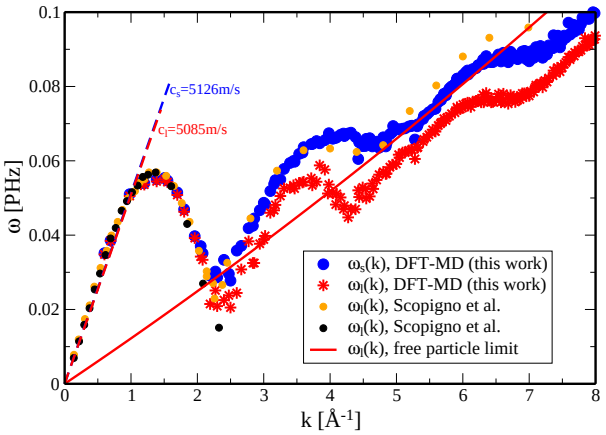

Figure 5. Dispersion relation for ion acoustic modes in liquid lithium. Calculations were performed at $T = 600$ K and $\rho = 0.495$ g/cm^3 for the positions of the side peaks of $S_{\rm ii}(k,\omega)$ (blue circles) and of the $J_{\rm l}(k,\omega)$ (red stars). Linear fits are shown in corresponding colors (dashed line). For the same conditions the free particle limit is shown (solid red line). Experimental dispersion relations of Scopigno *et al.* [22] are displayed for 600 K (black circles) and 475 K (orange circles).

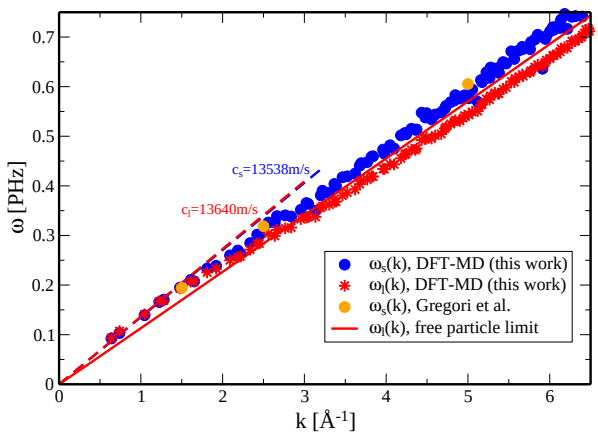

Figure 6. Same as Fig. 5 but for warm dense lithium at $T = 52220$ K and $\rho = 0.6$ g/cm^3. We compare additionally with an analytical solution of Gregori *et al.* [26] which applied frequency moment sum rules in a memory function formalism at the same temperature and ion density assuming an ionization degree of $Z_{\rm f} = 1.35$.

Moreover, the dynamic ion structure factor allows to extract material properties, i.e., relaxation times, the adiabatic exponent, but also the ion acoustic dispersion relation [16–19, 42, 50, 51]. For the two cases studied in this work, the dispersion relation of the collective excitations has been determined by analyzing the position of the side peaks with a triplet of three Lorentzian functions within the hydrodynamic model [18, 19, 42], see Figs. 5 and 6.

The calculated dispersion relation of liquid lithium at 600 K ($\Gamma = 157$) shown in Fig. 5 agrees with the experimentally determined one (only small k values available) [22] and shows for larger k the same systematic behavior according to the experimental dispersion relation for a slightly smaller temperature (475 K) [22]. We observe a non-linear dispersion relation, $\omega_s(k)$, characterized with minima at the peaks of the static structure factor in Fig. 1, i.e., the dispersion relation exhibits antiphase to the local order of the ions. At the boundary of the first pseudo-Brillouin zone at $k \approx 2.5$Å^{-1} the propagation of the acoustic modes is suppressed due to strong negative interference [52]. The slope of the linear part of the dispersion relation $\omega_s(k)$ at long-wavelengths provides the adiabatic speed of sound $c_{\rm s}$. In addition, the dispersion relation $\omega_l(k)$ of the longitudinal current correlation spectra $J_{\rm l}(k,\omega) = \omega^2/|k|^2 S_{\rm ii}(k,\omega)$ is shown in Fig. 5 and 6, where the apparent speed of sound, $c_{\rm l}$, is extracted from the linear part. We estimate an error of ∼10% for our calculations of the sound speeds related to a finite particle number in the simulation and the fitting procedure. In the liquid metal regime we determine $c_l = 5085$ m/s and $c_s = 5126$ m/s. These values agree with the apparent speed of sound $c_l = 5204$ m/s extracted from [52] and the adiabatic speed of sound estimated from experiments [53] $c_s = 4789$ m/s within 8%.

It is well known that at large k values the non-collective mode might be dominant. Therefore, the free particle dispersion relation [52] is also displayed using

$$\omega_{\rm l}(k) = \frac{\hbar k^2}{4m_{\rm i}} + \sqrt{\left(\frac{\hbar k^2}{4m_{\rm i}}\right)^2 + \frac{2k^2}{m_{\rm i}\beta}}. \qquad (9)$$

The intrinsic error of the dispersion relation from our analysis of the acoustic mode are increasing for larger k as their full width at half maximaum increases [54] and overlaps largely with the diffusive mode. We therefore obtain only a parallel slope to the free particle limit. We observe the dominance of the non-collective mode in liquid lithium above $k \geq 5$Å^{-1}.

On the other hand, in the WDM regime and due to less correlations ($\Gamma = 2$) compared with liquid lithium, the structure factor in Fig. 2 has no maxima. Hence, the dispersion relations in Fig. 6 show no depression for any k and are almost linear. In this case, also the dispersion relation of the free particles is linear, i.e., the second term under the root in Eq. (9) is dominant. Non-collective modes are dominant for $k \geq 3$Å^{-1}. Furthermore, we compare our dispersion relation with the position of the acoustic modes of the dynamic ion structure factor calculated via an analytical solution of Gregori *et al.* [26] and obtain agreement; where the frequency-dependent ion structure factor is calculated within the memory function formalism by satisfying a finite number of the sum

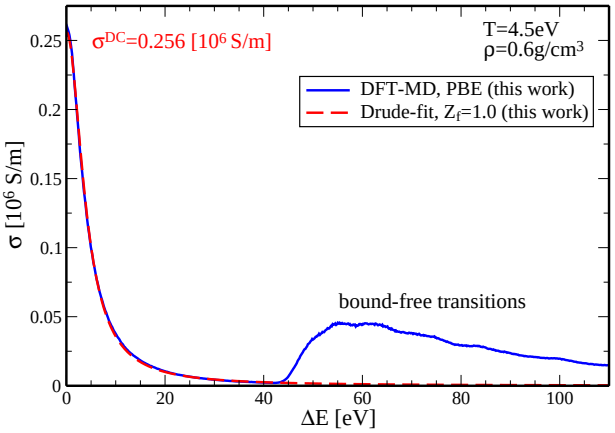

Figure 7. Dynamic electrical conductivity for warm dense lithium from DFT-MD simulations using the PBE functional (blue solid line). An ionization degree of $Z_\mathrm{f} = 1.0$ is determined from a fit of the Drude model (red dashed line).

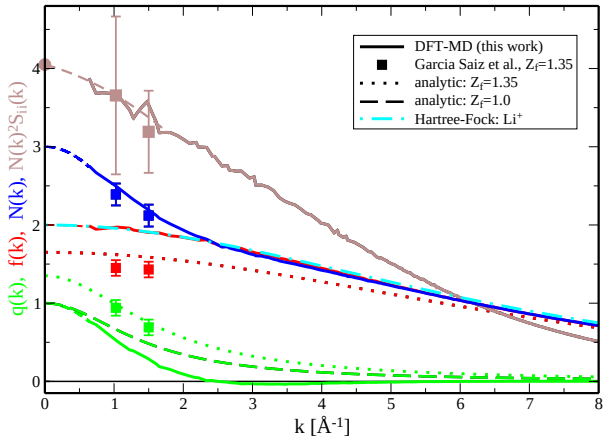

Figure 8. *Ion feature* (brown) in warm dense lithium at $T = 4.5$ eV and $\rho = 0.6$ g/cm^3 with the total form factor $N(k)$ (blue), atomic form factor $f(k)$ (red), and the form factor of screening electrons $q(k)$ (green) from DFT-MD simulations (solid line) compared with the values from [27] (boxes) and analytical calculations. The influence of the ionization degree, assuming $Z_\mathrm{f} = 1.0$ (dashed line) and $Z_\mathrm{f} = 1.35$ (dotted line) is shown within the analytical results using Debye-Hückel theory [55] for $q(k)$ and hydrogen-like wave functions [56] for $f(k)$. We compare also with $f(k)$ for Li^+ from Hartree-Fock [57] (dash-dotted).

rules. However, it is worth noting that the aspect ratio of the triplet peaks calculated by the analytical model is different from the DFT-MD results shown in Fig. 4. This can be due to approximations required for an analytical solution in [26], e.g., imposing a screened one-component plasma or the Debye-Hückel model for the zeroth moment, and applying a six-moment approximation.

V. COMPARISON WITH XRTS EXPERIMENTS ON WDM

XRTS probes the ionic correlations but is sensitive to the electronic structure. In this way, theoretical predictions for the total form factor $N(k)$ and the ion structure factor $S_{ii}(k)$ can be tested for WDM. The plasma parameters density and temperature are usually extracted from a best fit of the scattering spectrum using both the ion as well as the electron feature. Potential discrepancies could point to inhomogeneities or two-temperature states [29] that might be generated in such pump-probe experiments. Here, we compare our DFT-MD results with an XRTS experiment on warm dense Li [27].

A. *Ion feature*

DFT-MD simulations are carried out assuming a homogeneous target at $T = 4.5$ eV and $\rho = 0.6$ g/cm^3 –as extracted from the experiment– which yields in our case $Z_\mathrm{f} = 1.0$. Note that the ionization state could not be derived directly from the experiment via, e.g., the plasmon feature. Leaving the static ion structure factor $S_{ii}(k)$ as a free fit parameter, an ionization degree $Z_\mathrm{f}^\mathrm{fit} = 1.35$ has been predicted which is considerably higher than our result. To determine the ionization degree from DFT-MD we used two methods. First, we observe an energy gap of about 41 eV between the fully occupied bound states of the K-shell and the conducting L-shell. We therefore can discriminate the bound and free states by energy for the form factor calculation and determine $q(k \to 0) = Z_\mathrm{f} = 1.0$; see Eq. (6). Secondly, to benchmark this finding we calculated the dynamic electrical conductivity $\sigma(\omega)$ via the Kubo-Greenwood formula [58–62]; results are shown in Fig. 7.

The conductivity shows a Drude-like behavior up to an energy transfer of 41 eV, where we observe transitions from the bound 1s electrons to free states. Fitting the Drude model to the dynamic conductivity [63, 64] we extract the electron plasma frequency equivalent to an ionization degree of $Z_\mathrm{f} = 1.0$ and a DC conductivity of $\sigma^\mathrm{DC}(\omega \to 0) = 0.26 \times 10^6$ S/m. Note that the DC conductivity values and band gaps are dependent on the XC functional and are potentially modified by using higher order functionals, e.g., hybrid functionals [65].

In Fig. 8, we compare our results for the ion feature and the form factors with other theoretical models and the values given by García Saiz *et al.* [27]. The shown error bars of the experimental ion feature are determined utilizing the given error bars of $q(k)$, $f(k)$ and $S_\mathrm{ii}(k)$ in their paper. They calculated the screening cloud in terms of the electron-electron static response utilizing a modified Debye-Hückel model where static local field

corrections are accounted for. The bound form factor is calculated based on the Hartree-Fock self consistent field method [66]. We obtain a very good agreement for the ion feature and the total form factor by comparing our DFT-MD simulations with the experimental values at $k = 1.0$ Å^{-1} (40°) and $k = 1.5$ Å^{-1} (60°) [27]. Since the ionization degree fitted to the experiment is $Z_{\rm f}^{\rm fit} = 1.35$, differences in $q(k)$ and $f(k)$ for $k \to 0$ occur because $q(k \to 0) = Z_{\rm f}$, $f(k \to 0) = Z_{\rm b}$, and $N(k \to 0) = Z$ with $Z = Z_{\rm f} + Z_{\rm b} = 3$. In particular, the $q(k)$ from the DFT-MD simulations is lower than calculations in Debye-Hückel theory and shows antiscreening for $k = (2.5-5)$ Å^{-1}, as already found in other works [29, 38, 67]. The result of $q(k)$ in [27] is consistent with Debye-Hückel using $Z_{\rm f} = 1.35$. We compare our results for the bound form factor $f(k)$ also with calculations using analytical hydrogen-like wave functions [56] assuming $Z_{\rm f} = 1$ and Hartree-Fock [57] for Li^+ and find agreement. We mention here, that soft pseudo-potentials tend to delocalize wave functions of the bound electrons. To summarize, our DFT-MD simulations yield agreement with the measured ion feature and a consistent description of the contribution of free and bound electrons, thus allowing to infer the ionization degree based on first principles.

B. Scattering spectrum

The total scattering signal of a given density and temperature is accessible via the sum of the dynamic *ion feature* obtained from DFT-MD simulations and the dynamic *electron feature* determined here in Born-Mermin approximation (BMA) [6, 68] with an ionization degree from DFT-MD, convoluted with the instrumental broadening function.

The BMA considers electron-ion collisions via the collision frequency derived in Born approximation [69] and combined with a Mermin-like extension of the random phase approximation for the dielectric function [70]. For the calculation of the scattering spectrum, we neglect possible transitions between occupied and free electronic states. From our DFT calculations applying the PBE functional we expect the bound-free transitions to be only contributing to the scattering spectrum at photon energy shifts larger than the band gap; $\Delta\hbar\omega < -41$ eV. Using a more accurate functional the small bound-free contributions might be shifted even further out [65]. However, the calculation of the Chihara composites of the DSF using different theories for each scattering contribution can be overcome, i.e. by using only DFT-MD in combination with the wavelength dependency of an analytic dielectric function [65] or by using time-dependent DFT in the linear response regime [71]. For those examples no a priori assumption of the ionization degree is necessary. According to the experimental setup in [27], we report on the scattering signal for angles 40° and 60° in Fig. 9, where the DSF is convoluted with a Gaussian distribution with the full-width at half-maximum (FWHM) of 10.5 eV. In both cases, the calculated DFT-MD *ion feature* agrees with the measurement (except for a small statistical deviation at 60°, compare Fig. 8). The ion acoustic modes (Fig. 4) could not been resolved due to the broad instrumental function. The BMA electron feature calculated based on the averaged density and the averaged temperature used in DFT-MD simulations shows agreement with noisy experimental data. Our calculated electron feature has a higher amplitude than a synthetic spectrum [27], which is calculated from an inadequate EOS model in a radiation-hydrodynamic simulation. However, Garcia Saiz et al. extracted the plasma parameters $Z_{\rm f} = 1.35$, $\rho = 0.6$ g/cm^3, and T=4.5 eV not only from the rad-hydrodynamic simulations, but also from a best-fit model for the DSF and an ionization degree derived from their DFT-MD simulations for different densities (Fig. 3b in [27]); the latter method is not outlined and disagrees with our finding of $Z_{\rm f} = 1.0$.

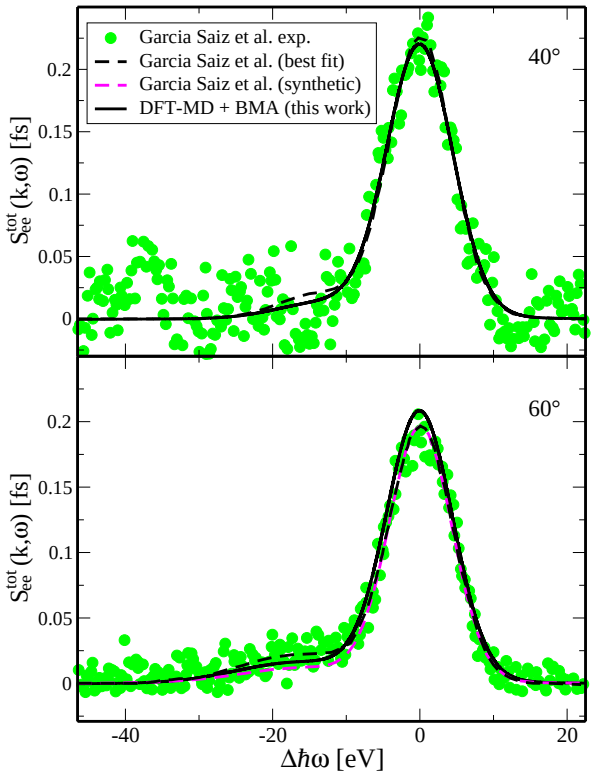

Figure 9. Dynamic structure factor at 40° and 60° versus the energy shift $\Delta\hbar\omega$. The calculated scattering signal (solid line) is based on the dynamic ion structure factor (Fig. 4) and the total form factor (Fig. 8) and the *electron feature* in BMA. The instrumental broadening is taken from [27]. It is compared to experimental scattering data (green circle), a best fit (black dashed line) [27] and a synthetic spectrum based on radiation-hydrodynamic simulations (magenta dashed line) [27].

We perform radiation-hydrodynamic simulations of the experimental setup utilizing the HELIOS code [72]. HELIOS features a Lagrangian reference frame where electrons and ions are assumed to be co-moving. Pressure contributions to the equation of motion stem from electrons, ions, and radiation. Separate ion and electron temperatures and a flux-limited Spitzer thermal conductivity are assumed. The non-local thermodynamic equilibrium kinetics are accounted for by solving multi-level atomic rate equations at each time step in the simulation. The laser energy is deposited via inverse bremsstrahlung as well as bound-bound and bound-free transitions using PROPACEOS equations of state [72]. Ionization was simulated using a multigroup ionization model based on the quotidian equation of state (QEOS) for strongly coupled plasmas [73]. PROPACEOS 4.2 calculates the ionization via a Saha model, while PROPACEOS 5.1 uses a Thomas-Fermi model as implemented in the QEOS [74]. The simulation parameters are taken from the experiment: The 250 μm solid thick lithium foil is driven with the 1 ns long Vulcan laser beam (frequency doubled to 512 nm) and flat-top focal spot size with average irradiance of $\approx 3 \times 10^{13}$ W/cm^2. The initial density and temperature of the target are 0.5 g/cm^3 and 0.025 eV, respectively.

The time-averaged (from 3 ns to 4 ns) plasma parameters as electron temperature, charge state, and mass density are displayed in Fig. 10. Our results show the same qualitative behavior compared to the HELIOS results provided by García Saiz *et al.*, except the ionization degree of the cold part of the target, i.e. right to the dashed line. We observe an average charge state in the cold part of 0.88, while the HELIOS simulations performed by García Saiz *et al.* predict a zero degree of ionization. The discrepancies are a consequence of using two different EOS models. The Saha-like EOS provides no ionization at room temperature as shown by García Saiz *et al.* On the other hand, and in this work, a Thomas-Fermi-like model considers pressure ionization and, consequently, a substantially higher ionization degree of 88% results. Hydrodynamic simulations based on Thomas-Fermi-like models have been found to be consistent with the measured data of warm dense lithium [75].

We find under-dense and hot plasmas at the surface up to ~ 40 μm in front of the target, followed by heated and compressed lithium, a shock-front within the target from $\sim$ 110 μm to 150 μm, and cold solid density at room temperature lithium behind the shock-front. The spatial averages of the time-averaged plasma parameters in Fig. 10 are as follows: The mass density is 0.5 g/cm^3. The electron and the ion density are 4.6×10^{22} cm^{-3} and 4.3×10^{22} cm^{-3}, respectively. The electron and ion temperature are 5.26 eV. In the inset of Fig. 10, we show the electron feature calculated using BMA considering these spatial-time averaged plasma parameters and the electron feature considering the inhomogeneity of the target at a scattering angle of 60°; the target is discretized into

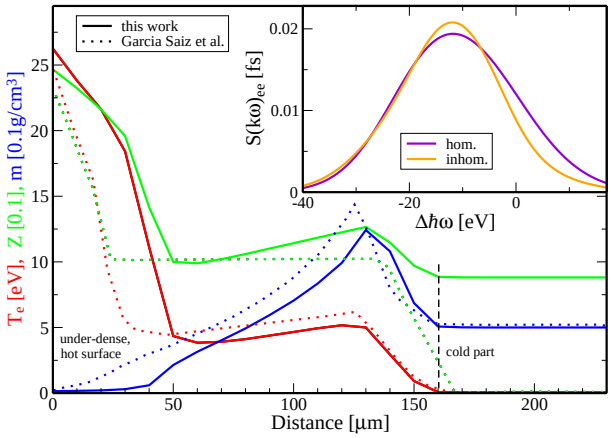

Figure 10. Time-averaged target parameters between 3 and 4 ns after the pump pulse simulated with HELIOS. In this work a Thomas-Fermi like EOS was considered (solid line) which is compared with results taken from [27] (dotted line) where a Saha-like EOS was utilized in the simulation. In the inset, the electron feature is calculated in BMA employing the spatial-time averaged plasma parameters (hom.) and inhomogeneous target parameters (inhom.)

25 cells and the shown signal is the average of Thomson scattering signals of all cells. The electron feature of each cell is calculated based on its local density and temperature; as inhomogeneity of the target affects the electron feature [28]. We are in this case neither on the stage of extracting all effects of density/temperature inhomogeneities for the available XRTS data nor diminish it from the noise. However, we point out, that in our case the inhomogeneity narrows the electron feature and increases its amplitude by 10%. Inhomogeneity effects, although they are small in this case, could be resolved using new XFELs with their unprecedented peak brightness and high repetition rate. It is worth reporting that a similar scenario could be applied using DFT-MD simulation to reveal the impact of the target inhomogeneity on the *ion feature*.

VI. CONCLUSION

In summary, we have determined the static and dynamic ion structure factor of liquid and warm dense lithium from first principles. We have extracted the dispersion relation for the ion acoustic modes and calculated the speed of sound. Using no input for the total form factor, the *ion feature* of warm dense lithium is calculated self-consistently within the DFT-MD simulations. We have found an excellent agreement with available experimental data [22, 27]. Based on radiation-hydrodynamic simulations, we have addressed the impact of inhomogeneities in the target on the scattering signal. These tend to increase the amplitude of the electron feature.

Applying the detailed balance relation to the ion acoustic mode and the electron feature provides the ion and electron temperature, respectively. Therefore, new high-brilliant and high-resolution x-ray sources such as LCLS and European XFEL will enable the investigation of non-equilibrium dynamics of warm dense matter in future experimental campaigns.

ACKNOWLEDGMENTS

We thank H. R. Rüter, P. Sperling and K.-U. Plagemann for helpful discussions. We acknowledge support of the DFG within the SFB 652 and by the BMBF within the FSP 302. The work was further supported by the DOE Office of Science, Fusion Energy Science under FWP 100182.

[1] N. Nettelmann, A. Becker, and R. Redmer, Astrophys. J. **750**, 52 (2012).
[2] M. French, A. Becker, W. Lorenzen, N. Nettelmann, M. Bethkenhagen, J. Wicht, and R. Redmer, Astrophys. J. Suppl. Ser. **202**, 11 (2012).
[3] T. Gastine, J. Wicht, L. Duarte, M. Heimpel, and A. Becker, Geophys. Res. Lett. **41**, 5410 (2014).
[4] J. D. Lindl, Phys. Plasmas **2**, 3933 (1995).
[5] M. J. Edwards et al., Physics of Plasmas **20**, 070501 (2013).
[6] S. H. Glenzer and R. Redmer, Rev. Mod. Phys. **81**, 1625 (2009).
[7] A. L. Kritcher, P. Neumayer, J. Castor, T. Döppner, R. W. Falcone, O. L. Landen, H. J. Lee, R. W. Lee, E. C. Morse, A. Ng, S. Pollaine, D. Price, and S. H. Glenzer, Science **322**, 69 (2008).
[8] L. B. Fletcher, H. J. Lee, T. Döppner, E. Galtier, B. Nagler, P. Heimann, C. Fortmann, S. LePape, T. Ma, M. Millot, A. Pak, D. Turnbull, D. A. Chapman, D. O. Gericke, J. Vorberger, T. White, G. Gregori, M. Wei, B. Barbrel, R. W. Falcone, C.-C. Kao, H. Nuhn, J. Welch, U. Zastrau, P. Neumayer, J. B. Hastings, and S. H. Glenzer, Nat Photon **9**, 274 (2015).
[9] C. Fortmann, T. Bornath, R. Redmer, H. Reinholz, G. Röpke, V. Schwarz, and R. Thiele, Laser Part. Beams **27**, 311 (2009).
[10] J. Chihara, J. Phys. Cond. Matter **12**, 231 (2000).
[11] S. H. Glenzer, O. L. Landen, P. Neumayer, R. W. Lee, K. Widmann, S. W. Pollaine, R. J. Wallace, G. Gregori, A. Höll, T. Bornath, R. Thiele, V. Schwarz, W.-D. Kraeft, and R. Redmer, Phys. Rev. Lett. **98**, 065002 (2007).
[12] R. Thiele, T. Bornath, C. Fortmann, A. Höll, R. Redmer, H. Reinholz, G. Röpke, A. Wierling, S. H. Glenzer, and G. Gregori, Phys. Rev. E **78**, 026411 (2008).
[13] P. Sperling, E. J. Gamboa, H. J. Lee, H. K. Chung, E. Galtier, Y. Omarbakiyeva, H. Reinholz, G. Röpke, U. Zastrau, J. Hastings, L. B. Fletcher, and S. H. Glenzer, Phys. Rev. Lett. **115**, 115001 (2015).
[14] K. Wünsch, J. Vorberger, G. Gregori, and D. O. Gericke, EPL **94**, 25001 (2011).
[15] D. Schiff, Phys. Rev. **186**, 151 (1969).
[16] J. P. Hansen and I. R. McDonald, Theory of Simple Liquids (Academic Press, London, 1986).
[17] P. Verkerk, J. Phys. Cond. Matter **13**, 7775 (2001).
[18] J.-F. Wax and T. Bryk, J. Phys. Cond. Matter **25**, 325104 (2013).
[19] N. M. Gill, R. A. Heinonen, C. E. Starrett, and D. Saumon, Phys. Rev E **91**, 063109 (2015).
[20] T. Scopigno, U. Balucani, G. Ruocco, and F. Sette, Phys. Rev. E **63**, 011210 (2000).
[21] H. Sinn and E. Burkel, J. Phys. Cond. Matter **8**, 9369 (1996).
[22] T. Scopigno, U. Balucani, A. Cunsolo, C. Masciovecchino, G. Ruocco, and F. Sette, Phil. Mag. B **79**, 2027 (1999).
[23] G. Monaco, A. Cunsolo, G. Pratesi, F. Sette, and R. Verbeni, Phys. Rev. Lett. **88**, 227401 (2002).
[24] A. A. van Well and L. A. de Graaf, Phys. Rev. A **32**, 2396 (1985).
[25] A. A. van Well, P. Verkerk, L. A. de Graaf, J.-B. Suck, and J. R. D. Copley, Phys. Rev. A **31**, 3391 (1985).
[26] G. Gregori and D. O. Gericke, Physics of Plasmas **16**, 056306 (2009).
[27] E. G. Saiz, G. Gregori, D. O. Gericke, J. Vorberger, B. Barbrel, R. J. Clarke, R. R. Freeman, S. H. Glenzer, F. Y. Khattak, M. Koenig, O. L. Landen, D. Neely, P. Neumayer, M. M. Notley, A. Pelka, D. Price, M. Roth, M. Schollmeier, C. Spindloe, R. L. Weber, L. van Woerkom, K. Wünsch, and D. Riley, Nat. Phys. **4**, 940 (2008).
[28] P. M. Kozlowski, B. J. B. Crowley, D. O. Gericke, S. P. Regan, and G. Gregori, Sci. Rep. **6** (2016).
[29] K.-U. Plagemann, H. R. Rüter, T. Bornath, M. Shihab, M. P. Desjarlais, C. Fortmann, S. H. Glenzer, and R. Redmer, Phys. Rev E **92**, 013103 (2015).
[30] G. Kresse and J. Hafner, Phys. Rev. B **47**, 558 (1993).
[31] G. Kresse and J. Hafner, Phys. Rev. B **49**, 14251 (1994).
[32] G. Kresse and J. Furthmüller, Phys. Rev. B **54**, 11169 (1996).
[33] P. E. Blöchl, Phys. Rev. B **50**, 17953 (1994).
[34] G. Kresse and D. Joubert, Phys. Rev. B **59**, 1758 (1999).
[35] J. P. Perdew, K. Burke, and M. Ernzerhof, Phys. Rev. Lett. **77**, 3865 (1996).
[36] S. Nosé, J. Chem. Phys. **81**, 511 (1984).
[37] A. Baldereschi, Phys. Rev. B **7**, 5212 (1973).
[38] H. Olbrich, H. Ruppersberg, and S. Steeb, Z. Naturforsch. **38 a**, 1328 (1983).
[39] J. Chihara, Phys. Rev. A **40**, 45077 (1989).

[40] T. Scopigno, U. Balucani, A. Cunsolo, C. Masciovecchio, G. Ruocco, F. Sette, and R. Verbeni, Eur. Phys. Lett. **50**, 189 (2000).

[41] T. Scopigno, U. Balucani, G. Ruocco, and F. Sette, Phys. Rev E **63**, 011210 (2000).

[42] H. R. Rüter and R. Redmer, Phys. Rev. Lett. **112**, 145007 (2014).

[43] S. Singh and K. Tankeshwar, Phys. Rev E **67**, 012201 (2003).

[44] T. G. White, S. Richardson, B. J. B. Crowley, L. K. Pattison, J. W. O. Harris, and G. Gregori, Phys. Rev. Lett. **111**, 175002 (2013).

[45] I. M. de Schepper, P. Verkerk, A. A. van Well, and L. A. de Graaf, Phys. Rev. Lett. **50**, 974 (1983).

[46] P. Mabey, S. Richardson, T. G. White, L. B. Fletcher, S. H. Glenzer, N. J. Hartley, J. Vorberger, D. O. Gericke, and G. Gregori, Nature Communications **8**, 14125 EP (2017).

[47] K. Appel, M. Nakatsutsumi, A. Pelka, G. Priebe, I. Thorpe, and T. Tschentscher, Plasma Physics and Controlled Fusion **57**, 014003 (2015).

[48] C. Bostedt, S. Boutet, D. M. Fritz, Z. Huang, H. J. Lee, H. T. Lemke, A. Robert, W. F. Schlotter, J. J. Turner, and G. J. Williams, Rev. Mod. Phys. **88**, 015007 (2016).

[49] S. H. Glenzer, L. B. Fletcher, E. Galtier, B. Nagler, R. Alonso-Mori, B. Barbrel, S. B. Brown, D. A. Chapman, Z. Chen, C. B. Curry, F. Fiuza, E. Gamboa, M. Gauthier, D. O. Gericke, A. Gleason, S. Goede, E. Granados, P. Heimann, J. Kim, D. Kraus, M. J. MacDonald, A. J. Mackinnon, R. Mishra, A. Ravasio, C. Roedel, P. Sperling, W. Schumaker, Y. Y. Tsui, J. Vorberger, U. Zastrau, A. Fry, W. E. White, J. B. Hasting, and H. J. Lee, Journal of Physics B: Atomic, Molecular and Optical Physics **49**, 092001 (2016).

[50] T. Bryk and G. Ruocco, Molecular Physics **111**, 3457 (2013).

[51] T. Scopigno, U. Balucani, G. Ruocco, and F. Sette, Phys. Rev. Lett. **85**, 4076 (2000).

[52] T. Scopigno, U. Balucani, G. Ruocco, and F. Sette, J. Phys. Cond. Matter **12**, 8009 (2000).

[53] S. Blairs, Phys. Chem. Liq. **44**, 597 (2006).

[54] J. Clérouin, P. Arnault, C. Ticknor, J. D. Kress, and L. A. Collins, Phys. Rev. Lett. **116**, 115003 (2016).

[55] P. Sperling, R. Thiele, B. Holst, C. Fortmann, S. Glenzer, S. Toleikis, T. Tschentscher, and R. Redmer, High Energy Dens. Phys. **7**, 145 (2011).

[56] L. Pauling and J. Sherman, Zeitschrift für Kristallographie **81**, 1 (1932).

[57] E. Prince, ed., International Tables for Crystallography, Vol. C (John Wiley & Sons, New York, 2006).

[58] R. Kubo, J. Phys. Soc. Jpn. **12**, 570 (1957).

[59] D. A. Greenwood, Proc. Phys. Soc. **71**, 585 (1958).

[60] M. P. Desjarlais, J. D. Kress, and L. A. Collins, Phys. Rev. E **66**, 025401 (2002).

[61] A. Kietzmann, R. Redmer, M. P. Desjarlais, and T. R. Mattsson, Phys. Rev. Lett. **101**, 070401 (2008).

[62] M. French, T. R. Mattsson, and R. Redmer, Phys. Rev. B **82**, 174108 (2010).

[63] V. Vlček, N. de Koker, and G. Steinle-Neumann, Phys. Rev. B **85**, 184201 (2012).

[64] K.-U. Plagemann, P. Sperling, R. Thiele, M. P. Desjarlais, C. Fortmann, T. Döppner, H. J. Lee, S. H. Glenzer, and R. Redmer, New J. Phys. **14**, 055020 (2012).

[65] B. B. L. Witte, L. B. Fletcher, E. Galtier, E. J. Gamboa, H.-J. Lee, U. Zastrau, R. Redmer, S. H. Glenzer, and P. Sperling, submitted (2016).

[66] G. Gregori, A. Ravasio, A. Holl, S. Glenzer, and S. Rose, High Energy Density Physics **3**, 99 (2007).

[67] D. O. Gericke, J. Vorberger, K. Wünsch, and G. Gregori, Phys. Rev. E **81**, 065401 (2010).

[68] A. Höll, T. Bornath, L. Cao, T. Döppner, S. Düsterer, E. Förster, C. Fortmann, S. H. Glenzer, G. Gregori, T. Laarmann, K.-H. Meiwes-Broer, A. Przystawik, P. Radcliffe, R. Redmer, H. Reinholz, G. Röpke, R. Thiele, J. Tiggesbäumker, J. Toleikis, N. X. Truong, T. Tschentscher, I. Uschmann, and U. Zastrau, High Energy Dens. Phys. **3**, 120 (2007).

[69] H. Reinholz, R. Redmer, G. Röpke, and A. Wierling, Phys. Rev. E **62**, 5648 (2000).

[70] A. Selchow, G. Röpke, and A. Wierling, Contrib. Plasma Phys. **42**, 43 (2002).

[71] A. D. Baczewski, L. Shulenburger, M. P. Desjarlais, S. B. Hansen, and R. J. Magyar, **116**, 115004 (2016).

[72] J. J. MacFarlane, I. E. Golovkin, and P. R. Woodruff, J. Quant. Spectrosc. Radiat. Transfer **99**, 381 (2006).

[73] R. M. More, K. H. Warren, D. A. Young, and G. B. Zimerman, Phys. Fluids **31**, 3059 (1988).

[74] U. Zastrau, P. Sperling, A. Becker, T. Bornath, R. Bredow, T. Döppner, S. Dziarzhytski, T. Fennel, L. B. Fletcher, E. Förster, C. Fortmann, S. H. Glenzer, S. Göde, G. Gregori, M. Harmand, V. Hilbert, B. Holst, T. Laarmann, H. J. Lee, T. Ma, J. P. Mithen, R. Mitzner, C. D. Murphy, M. Nakatsutsumi, P. Neumayer, A. Przystawik, S. Roling, M. Schulz, B. Siemer, S. Skruszewicz, J. Tiggesbäumker, S. Toleikis, T. Tschentscher, T. White, M. Wöstmann, H. Zacharias, and R. Redmer, Phys. Rev. E **90**, 013104 (2014).

[75] N. L. Kugland, G. Gregori, S. Bandyopadhyay, C. M. Brenner, C. R. D. Brown, C. Constantin, S. H. Glenzer, F. Y. Khattak, A. L. Kritcher, C. Niemann, A. Otten, J. Pasley, A. Pelka, M. Roth, C. Spindloe, and D. Riley, Phys. Rev. E **80**, 066406 (2009).